

Edge assisted epitaxy of $CsPbBr_3$ nanoplates on Bi_2O_2Se nanosheets for enhanced photoresponse

Haotian Jiang(蒋浩天), Xing Xu(徐兴), Chao Fan(樊超), Beibei Dai(代贝贝),Zhuodong Qi(亓卓栋), Sha Jiang(蒋莎), Mengqiu Cai(蔡孟秋), and Qinglin Zhang(张清林)

Citation: Chin. Phys. B, 2022, 31 (**4**): 048102. DOI: 10.1088/1674-1056/ac2b20
Journal homepage: http://cpb.iphy.ac.cn; http://iopscience.iop.org/cpb

What follows is a list of articles you may be interested in

Distribution of donor states on the surfaceof AlGaN/GaN heterostructures

Yue-Bo Liu(柳月波), Hong-Hui Liu(刘红辉), Jun-Yu Shen(沈俊宇), Wan-Qing Yao(姚婉青), Feng-Ge Wang(王风格), Yuan Ren(任远), Min-Jie Zhang(张敏杰), Zhi-Sheng Wu(吴志盛), Yang Liu(刘扬), and Bai-Jun Zhang(张佰君)

Chin. Phys. B, 2021, 30 (**12**): 128102. DOI: 10.1088/1674-1056/ac0792

Edge-and strain-induced band bending in bilayer-monolayer Pb_2Se_3 heterostructures

Peng Fan(范朋), Guojian Qian(钱国健), Dongfei Wang(王东飞), En Li(李恩), Qin Wang(汪琴), Hui Chen(陈辉), Xiao Lin(林晓), and Hong-Jun Gao(高鸿钧)

Chin. Phys. B, 2021, 30 (**1**): 018105. DOI: 10.1088/1674-1056/abcf92

Effect of growth temperature of $GaAs_xSb_{1-x}$ metamorphic buffer layer on electron mobility of InAs/AlSb heterostructures grown on Si substrate

Jing Zhang(张静), Hong-Liang Lv(吕红亮), Hai-Qiao Ni(倪海桥), Shi-Zheng Yang(杨施政), Xiao-Ran Cui(崔晓然), Zhi-Chuan Niu(牛智川), Yi-Men Zhang(张义门), Yu-Ming Zhang(张玉明)

Chin. Phys. B, 2019, 28 (**11**): 118102. DOI: 10.1088/1674-1056/ab4d49

Superlubricity enabled dry transfer of non-encapsulated graphene

Zhe Ying(应哲), Aolin Deng(邓奥林), Bosai Lyu(吕博赛), Lele Wang(王乐乐), Takashi Taniguchi, Kenji Watanabe, Zhiwen Shi(史志文)

Chin. Phys. B, 2019, 28 (**2**): 028102. DOI: 10.1088/1674-1056/28/2/028102

High-performance InAlGaN/GaN enhancement-mode MOS-HEMTs grown by pulsed metal organic chemical vapor deposition

Ya-Chao Zhang(张雅超), Zhi-Zhe Wang(王之哲), Rui Guo(郭蕊), Ge Liu(刘鸽), Wei-Min Bao(包为民), Jin-Cheng Zhang(张进成), Yue Hao(郝跃)

Chin. Phys. B, 2019, 28 (**1**): 018102. DOI: 10.1088/1674-1056/28/1/018102

Edge assisted epitaxy of $CsPbBr_3$ nanoplates on Bi_2O_2Se nanosheets for enhanced photoresponse

Haotian Jiang(蒋浩天), Xing Xu(徐兴), Chao Fan(樊超), Beibei Dai(代贝贝), Zhuodong Qi(亓卓栋), Sha Jiang(蒋莎), Mengqiu Cai(蔡孟秋), and Qinglin Zhang(张清林)†

Key Laboratory for Micro-/Nano-Optoelectronic Devices of Ministry of Education, School of Physics and Electronics, Hunan University, Changsha 410082, *China*

(Received 15 May 2021; revised manuscript received 23 September 2021; accepted manuscript online 29 September 2021)

Bi_2O_2Se has been proved to be a promising candidate for electronic and optoelectronic devices due to their unique physical properties. However, it is still a great challenge to construct the heterostructures with direct epitaxy of hetero semiconductor materials on Bi_2O_2Se nanosheets. Here, a two-step chemical vapor deposition (CVD) route was used to directly grow the $CsPbBr_3$ nanoplate-Bi_2O_2Se nanosheet heterostructures. The $CsPbBr_3$ nanoplates were selectively grown on the Bi_2O_2Se nanosheet along the edges, where the dangling bonds provide the nucleation sites. The epitaxial relationships between $CsPbBr_3$ and Bi_2O_2Se were determined as $[200]_{Bi_2O_2Se}||[110]_{CsPbBr_3}$ and $[110]_{Bi_2O_2Se}||[200]_{CsPbBr_3}$ by transmission electron microscopy characterization. The photoluminescence (PL) results reveal that the formation of heterostructures results in the remarkable PL quenching due to the type-I band arrangement at $CsPbBr_3/Bi_2O_2Se$ interface, which was confirmed by ultraviolet photoelectron spectroscopy (UPS) and Kelvin probe measurements, and makes the photogenerated carriers transfer from $CsPbBr_3$ to Bi_2O_2Se. Importantly, the photodetectors based on the heterostructures exhibit a 4-time increase in the responsivity compared to those based on the pristine Bi_2O_2Se sheets, and the fast rise and decay time in microsecond. These results indicate that the direct epitaxy of the $CsPbBr_3$ plates on the Bi_2O_2Se sheet may improve the optoelectronic performance of Bi_2O_2Se based devices.

Keywords: Bi_2O_2Se, heterostructures, photogenerated carriers, photoresponse

PACS: 81.05.zx, 68.37.Lp, 72.20.Jv, 85.30.De **DOI:** 10.1088/1674-1056/ac2b20

1. Introduction

Two-dimensional (2D) semiconductor materials have attracted extensive research interest for both the fundamental physics researches and the practical applications in electronic and optoelectronic devices, due to their unique optical and electrical properties.[1–8] Recently, Bi_2O_2Se, an emerging 2D material, has been proved to possess typical narrow bandgap, high carrier mobility and superior air stability, which makes it a promising candidate for high-performance devices, such as field effect transistors (FETs), broadband photodetectors (PDs) and ultrafast photodetection.[9–20] Because the heterointerfaces directly determine the operation of modern electronic devices,[21–24] the fabrication of Bi_2O_2Se-based heterostructures is crucially important for practical applications of the related devices.

Up to date, the combination of Bi_2O_2Se with other 2D materials including graphene, $MoSe_2$ and WSe_2 has been applied to realize the multifunctional electronics, e.g., the bidirectional all-optical synapses or broadband PDs with high light on/off ratio and fast response.[25–28] Although the high-quality interface may be achieved with two disparate layered materials (2D–2D heterostructures) due to their atomically smooth surfaces without dangling bonds, the limited quantity greatly restricts them to meet the requirements of various functional applications. Moreover, these reported Bi_2O_2Se-based 2D–2D heterostructures were fabricated with the manual micromanipulation techniques assisted by the optical microscope, which still suffers from the poor positional controllability and low efficiency.[29,30] Consequently, the highly efficient integration of 2D materials with non-layered ones is indispensable to the extended applications beyond 2D–2D heterostructures. Luo *et al.* reported that the sensitization of Bi_2O_2Se nanoplates with PbSe quantum dots (QDs) could expand the photoresponse spectral range of Bi_2O_2Se-based PDs to the wavelength of 2 μm with the response time 300 times faster than PbSe QDs.[31] Although a remarkable enhancement to the responsivity may be obtained with the sensitization due to the photogating effect, the grain boundaries among the stacked QDs as well as the weakly interfacial coupling between QDs and the layered materials may inevitably decrease the carrier transfer efficiency from the sensitizer to the channel material.[32–34] The epitaxial growth of non-layered semiconductors on 2D materials exhibits great potential in efficiently constructing the 2D-based heterostructures high-quality heterointerface, where the dangling-bond-free surfaces of the layered structures are favorable to the growth of epitaxial materials on it without strict lattice match.[3,35–37] Although the various non-layered materials have been epitaxially grown on the traditional 2D materials,[33,38,39] it is still challenging to direct epitaxy of them on Bi_2O_2Se nanosheets.

†Corresponding author. E-mail: qinglin.zhang@hnu.edu.cn

© 2022 Chinese Physical Society and IOP Publishing Ltd

$CsPbBr_3$, one of the all inorganic metal halide perovskite, has been proved to possess strong visible light absorption, bipolar transport, long carrier diffusion distance, etc., which is ideal for the light light-absorbing layer.[22,40–42] Furthermore, the integration of $CsPbBr_3$ with 2D materials, such as MoS_2, WSe_2 or WS_2, may result in the ultrafast charge transfer from $CsPbBr_3$ to the layered materials, which is favorable for the high performance optoelectronic devices based on 2D materials.[43,44] Noh *et al.* fabricated the devices with MoS_2–$CsPbBr_3$ quantum dots hybrid which exhibited ~ 4 times and ~ 17 times increase, respectively, in the field effect mobility and photoresponsivity under light irradiation than those prepared without the perovskite QDs and without light irradiation.[45] Zhang *et al.* reported a photodetector based on $CsPbBr_3$ nanocrystal/monolayer MoS_2, with a high photoresponsivity of 6.40×10^5 $mA{\cdot}W^{-1}$, an external quantum efficiency of $1.50 \times 10^5\%$, and a specific detectivity of 3.38×10^{11} Jones at zero gate voltage.[46] Although great progress has been made on the theory and application of the hybrids of $CsPbBr_3$-layered transition metal dichalcogenides, the study of the heterostructures of $CsPbBr_3$–Bi_2O_2Se is still in the initial stage.

Here, we report the high-quality $CsPbBr_3$ nanoplate-Bi_2O_2Se nanosheet heterostructure synthesized via a two-step chemical vapor deposition (CVD) route. $CsPbBr_3$ nanoplates were selectively grown at the edge of the Bi_2O_2Se sheet, when the pre-synthesized Bi_2O_2Se nanoplates were annealed in the evaporated CsBr and $PbBr_2$ atmosphere. The epitaxial relationship between $CsPbBr_3$ plates and the Bi_2O_2Se sheets were verified to be $[200]_{Bi_2O_2Se}||[110]_{CsPbBr_3}$ and $[110]_{Bi_2O_2Se}||[200]_{CsPbBr_3}$ by a transmission electron microscopy (TEM). The control experiments demonstrate the dangling bonds at the edge of Bi_2O_2Se sheets play a critical role in the nucleation of $CsPbBr_3$. The microphotoluminescence (μ-PL) characterizations reveal that the contact of $CsPbBr_3$ with Bi_2O_2Se results in a significant PL quenching. The ultraviolet photoelectron spectroscopy (UPS) and Kelvin probe measurements reveal the type-I band alignment at the hetero-interface, which makes the photogenerated carrier transfer from $CsPbBr_3$ to Bi_2O_2Se and hence the PL quenching. Importantly, the photodetectors based on the heterostructures have the responsivity of 7.7 A/W, which is more than 4 times higher than that of the devices based on the pristine Bi_2O_2Se (1.8 A/W). This can be contributed to the high absorption coefficient of $CsPbBr_3$ and the efficient carrier transfer from $CsPbBr_3$ to Bi_2O_2Se. Additionally, the devices based on the heterostructures exhibit fast response time of 4.4 ms and 2.8 ms for the rise and decay time, respectively. The direct epitaxy of $CsPbBr_3$ plate on Bi_2O_2Se sheet paves the way to fabricating the Bi_2O_2Se based heterostructures with high efficiency, which promotes the practical application of Bi_2O_2Se in optoelectronic devices.

2. Experimental details

Sample preparation $CsPbBr_3$ nanoplate-Bi_2O_2Se heterostructures were synthesized by a two-step CVD route. Firstly, Bi_2O_2Se nanosheets were synthesized on a freshly cleaved mica substrate by a furnace with 1-inch diameter quartz tube. The Bi_2O_3 powder was put in the center of the heat zone, Bi_2Se_3 powder was put upstream 10 cm away from the center, and the mica was placed downstream 12 cm away from the center. Before the growth, 200 sccm N_2 gas flow was used to flush the system for 30 min to exhaust air. Then, the furnace was heated to 620 °C and kept constant for 30 min to synthesize Bi_2O_2Se nanosheets. In the whole process, the pressure in the furnace was controlled at about 2500 Pa. Secondly, $CsPbBr_3$ nanoplate-Bi_2O_2Se nanosheet heterostructures were synthesized by annealing the pre-grown Bi_2O_2Se nanosheet in the evaporated $PbBr_2$ and CsBr atmosphere. The mixed $PbBr_2$ and CsBr powders (molar ratio 1:1) was placed at the center of the heating zone, and the pre-grown Bi_2O_2Se nanosheets were placed at the downstream. Then the furnace was heated to 550 °C and kept for 10 min to grow $CsPbBr_3$ nanoplate on Bi_2O_2Se nanosheet.

Characterizations The morphologies and crystal structure of $CsPbBr_3$ nanoplate-Bi_2O_2Se heterostructures were characterized by an optical microscope, SEM (Hitachi, S-4800), XRD (Shimadzu, XRD-6100), and TEM (FEI, Tecnai G2 F20). The Raman and PL measurements were performed with a confocal microscope (Witec Alpha 300) under the excitation of a focused 473 nm laser.

Device fabrication The device of $CsPbBr_3$ nanoplate-Bi_2O_2Se was prepared *in situ* on the grown mica substrate. Two small pieces of Sn/Bi alloy (melting point: about 148 °C) foils were manipulated with a micro probe under the optical microscope to contact with the Bi_2O_2Se sheet to act as the source and drain. Then, the devices were annealed at 150 °C for 20 s to improve the electrical contact. Finally, the electronic characteristics of the obtained devices were measured by a probe table with a semiconductor parameter analyzer (Agilent, B4155C) and the photoresponse time was recorded by an oscilloscope (TDS5054B).

3. Results and discussion

Figure 1(a) shows the optical microscope image of a representative Bi_2O_2Se nanosheet grown on the mica substrate. The quadrate sheet with the side length of ~ 25 microns agrees well with the tetragonal phase of Bi_2O_2Se.[20,48] After the pre-synthesized Bi_2O_2Se sheets were annealed in the evaporated CsBr and $PbBr_2$ atmosphere, $CsPbBr_3$ square nanoplates with the side length of several microns were only grown at the edges

of Bi_2O_2Se sheets (see Figs. 1(b) and S1 in the supporting information), while the inner area of the Bi_2O_2Se sheets keeps the clean surface as the pristine ones, which indicates that the edges of Bi_2O_2Se sheets play an important role in the nucleation of $CsPbBr_3$. Interestingly, a diagonal of each of the $CsPbBr_3$ plates is parallel with the side of Bi_2O_2Se sheet. In consideration of the cubic phase of $CsPbBr_3$ and tetragonal phase of Bi_2O_2Se, it can be deduced that the $[110]_{CsPbBr_3}$ is parallel with $[100]_{Bi_2O_2Se}$, which will be further discussed latter. The thickness of the Bi_2O_2Se sheet and epitaxial $CsPbBr_3$ plate were measured by an atomic force microscopy (AFM) to be about 25 and 85 nm, respectively (see Fig. S2 in the supporting information). Figure 1(c) gives the locally amplified scanning electron microscope (SEM) image of the heterostructure. The corresponding elemental mappings (see Fig. 1(d)) clearly show that Bi and Se elements distribute uniformly across the entire upper part, while Pb and Br only distribute in the square area with its diagonal parallel with the side of Bi_2O_2Se plate, which results in one half of the $CsPbBr_3$ plate being on the Bi_2O_2Se (upper part) and the other half being on the mica (lower part). To check the crystal phases, the x-ray diffraction (XRD) patterns of the obtained heterostructures were measured (shown in Fig. 1(c)). The diffraction peaks can be respectively indexed to cubic $CsPbBr_3$ (PDF# 75-0412) and tetragonal Bi_2O_2Se (PDF# 73-1316), where the sharp diffraction peaks demonstrate the high crystal quality of the as-grown sample. Additionally, only the peaks of $\{200\}_{sPbBr_3}$ and $\{002\}_{Bi_2O_2Se}$ can be observed, indicating that the $CsPbBr_3$ plates were grown with the $(200)_{CsPbBr_3}$ plane interfacing with the surface of $(002)_{Bi_2O_2Se}$.

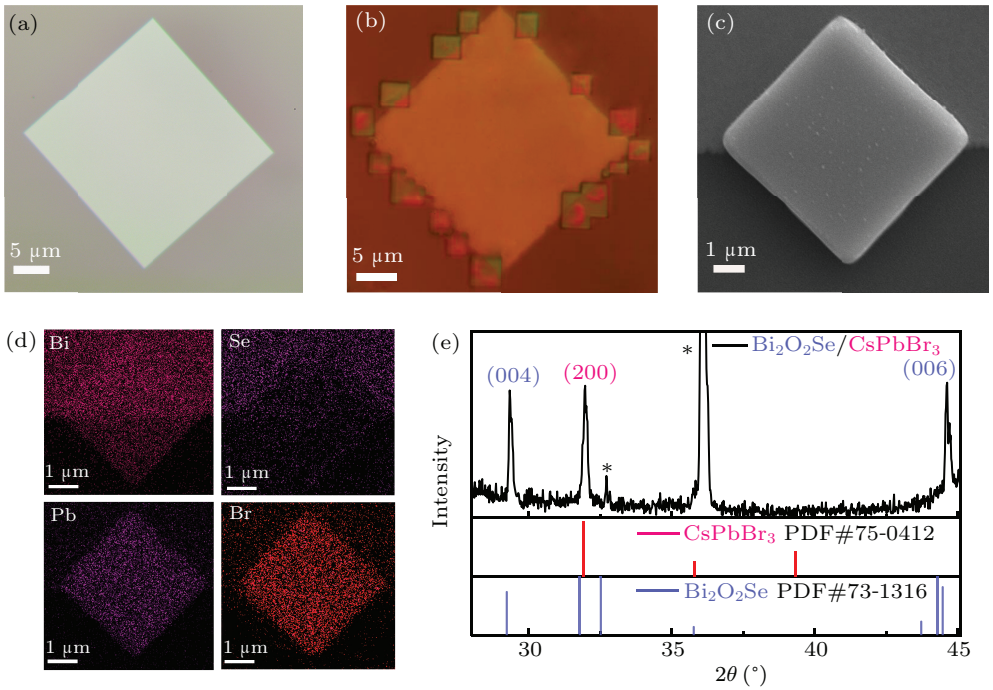


Fig. 1. (a) Optical microscope image of a representative Bi_2O_2Se nanoplate grown on a mica. (b) Optical microscopy images of $CsPbBr_3$ nanoplate-Bi_2O_2Se nanosheet heterostructures grown on a mica. (c) Locally amplified SEM image of the heterostructure. (d) EDS mapping of Bi, Se, Pb and Br elements measured from the area of (b). (e) XRD spectra of the heterostructures.

To reveal the detailed epitaxial relationships between the $CsPbBr_3$ plates and the Bi_2O_2Se sheets, TEM were used to check their microstructures. Figure 2(a) shows the low-magnification TEM image of the $CsPbBr_3$–Bi_2O_2Se heterostructure transferred onto a Cu grid. It can be seen that $CsPbBr_3$ plate contacts with the edges of Bi_2O_2Se sheet with an angle of 45° between the sides of these two phases, which is consistent with the results in above optical microscope and SEM images. Figures 2(b) and 2(c) are the high-resolution TEM (HRTEM) images corresponding to the Bi_2O_2Se and $CsPbBr_3$ region marked by the solid- and dotted-line rectangle in Fig. 2(a), respectively. The lattice spacing can be measured to be 0.195 and 0.421 nm for $(200)_{Bi_2O_2Se}$ (Fig. 2(b)) and $(110)_{CsPbBr_3}$, respectively (Fig. 2(c)). The corresponding selected-area electron diffraction (SAED) patterns (insets in Figs. 2(b) and 2(c)) further confirm the tetragonal and cubic crystal for the Bi_2O_2Se and $CsPbBr_3$, respectively. Figure 2(d) gives the SAED pattern measured at the position marked by the circle in Fig. 2(a) with the electrons incident along the $[001]_{Bi_2O_2Se}$ and $[001]_{CsPbBr_3}$ direction. Two sets of spots can be clearly distinguished for tetragonal Bi_2O_2Se (red square) and cubic $CsPbBr_3$ (green square), respectively. The epitaxial relationships between Bi_2O_2Se and $CsPbBr_3$ can be deduced to be $[200]_{Bi_2O_2Se}||[110]_{CsPbBr_3}$ and $[110]_{Bi_2O_2Se}||[200]_{CsPbBr_3}$ in two in-plane directions. This directional relationships are consistent with the nearly same lattice mismatch factors (defined as $f = [(d_{Bi_2O_2Se} - d_{CsPbBr_3})/d_{Bi_2O_2Se} \times 100\%)]$ of $[200]_{Bi_2O_2Se}||[220]_{CsPbBr_3}$

(−6.75%) and $[110]_{Bi_2O_2Se}||[200]_{CsPbBr_3}$ (−6.75%), where $d_{Bi_2O_2Se(200)} = 0.195$ nm, $d_{Bi_2O_2Se(110)} = 0.275$ nm (PDF# 73-1316), $d_{CsPbBr_3(220)} = 0.207$ nm and $d_{CsPbBr_{3(200)}} = 0.294$ nm (PDF# 75-0412). These result in the same energy barriers for aligning the adatoms of $CsPbBr_3$ along $[200]_{Bi_2O_2Se}$ and $[110]_{Bi_2O_2Se}$, which contribute to the formation of square $CsPbBr_3$ plate on the Bi_2O_2Se sheet (see the atomic arrangement schematic of the heterostructure in Fig. 2(e)).

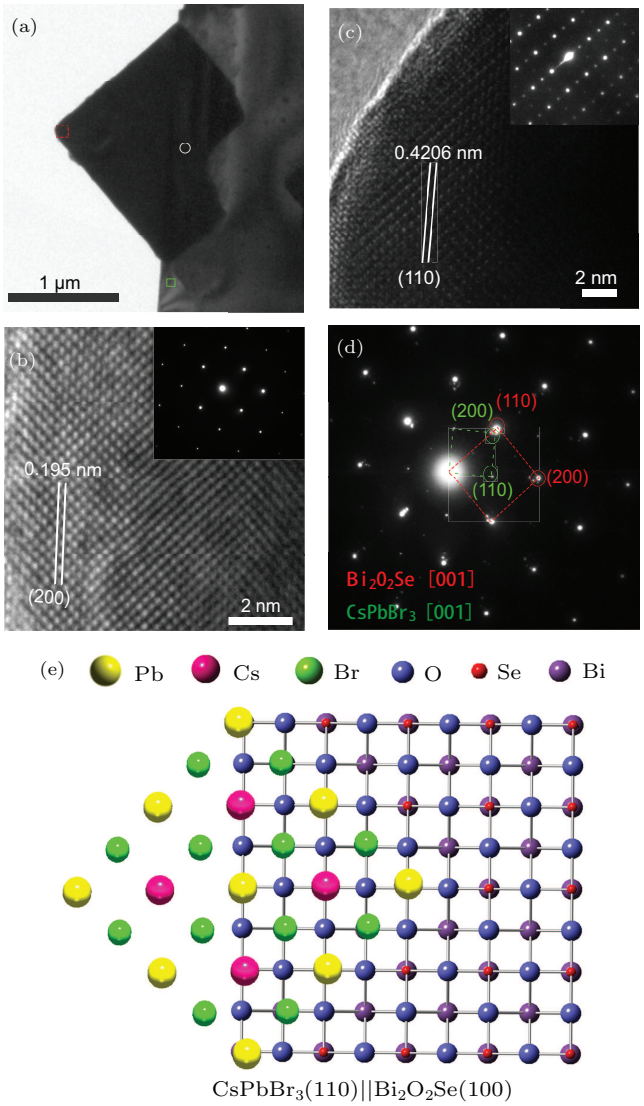


Fig. 2. (a) Low-magnification TEM image of $CsPbBr_3$ nanoplate-Bi_2O_2Se heterostructure transferred onto a Cu grids. (b) HRTEM image of the area marked with solid line rectangle in (a). Inset: The corresponding SAED pattern. (c) HRTEM image of the area marked with dotted line rectangle in (a). Inset: The corresponding SAED pattern. (d) SAED pattern measured at the position marked with a circle in (a). (e) Atomic arrangement schematic of the $CsPbBr_3$ nanoplate-Bi_2O_2Se nanosheet viewed from $[001]_{Bi_2O_2Se}||[001]_{CsPbBr_3}$.

To further confirm the initial nucleation location of the $CsPbBr_3$ plates, the Bi_2O_2Se film with millimeter size was used as the epitaxial substrate. As shown in Fig. S3(a), there are many cracks in the film, which may be resulted from the large strain generated during the growth process. Interestingly, after the film was annealed in the evaporated CsBr and $PbBr_2$ atmosphere, many $CsPbBr_3$ plates appear and all of them are selectively grown along the cracks with the same orientations (see Fig. S3(b)). Because both sides of the crack are Bi_2O_2Se, this result clearly reveals that the $CsPbBr_3$ plates primarily nucleate at the edge of Bi_2O_2Se sheet. We contribute this to the unsaturated atoms at the edges of Bi_2O_2Se sheets (see the crystal structure schematic in Figs. S4) which provide the nucleation sites for $CsPbBr_3$, and then promote the growth of the plates on Bi_2O_2Se surface according to the defined epitaxial relationships. Figure S5 gives the SEM images of the $CsPbBr_3$ plates grown on thin and thick Bi_2O_2Se sheets, measured with the tilted view. For the thin Bi_2O_2Se sheet (Fig. S5(b)), the square $CsPbBr_3$ plates stretch across the edge of the Bi_2O_2Se sheet and contact with both mica and Bi_2O_2Se. However, for the thick Bi_2O_2Se sheet with the thickness of about 2 μm (Fig. S5(a)), right triangle $CsPbBr_3$ plates were only grown on the mica with the right-angle side contacting with the side wall of Bi_2O_2Se sheet, where steps were formed due to the larger thickness of Bi_2O_2Se sheet than that of $CsPbBr_3$ plates. These further reveal that the initial nucleation of $CsPbBr_3$ was assisted by the edges of Bi_2O_2Se sheets, where the adatoms of $CsPbBr_3$ connect with the dangling bonds at the edge of Bi_2O_2Se sheets with $(200)_{Bi_2O_2Se}||(110)_{CsPbBr_3}$. The formation of square or right-triangle shape $CsPbBr_3$ plates is thermodynamically favorable, because the exposure of $\{001\}_{CsPbBr_3}$ results in the lowest surface energy for a cubic crystal.[22]

It should be noted that all the $CsPbBr_3$ plates were aligned along the edge of Bi_2O_2Se sheet (see Figs. 1 and S1), which is quite different from the epitaxy of $CsPbBr_3$ nanowires on the surface of Bi_2O_2Se sheets with the epitaxial relationship of $[200]_{Bi_2O_2Se}||[001]_{CsPbBr_3}$.[49] We contribute these to the various growth modes controlled by the growth conditions. The wires nucleated in the inner part of Bi_2O_2Se sheets where the surface of (001) plane is free of dangling bonds, while the plates were grown at the edge of Bi_2O_2Se sheets with many dangling bonds. Generally, the growth of epilayer on a substrate with chemical bonds requires to overcome much higher energy barrier than that with van der Waals (vdW) force.[50] Consequently, the wires were grown by a vertically physical vapor deposition method with low evaporation (330 °C) and growth (220 °C) temperature, which resulted in the low precursor supersaturation and low adatom diffusion rate. Differently, the plates were grown by a horizontally chemical vapor deposition routes with high evaporation (550 °C) and growth (320 °C) temperature, which may lead to high precursor super staturation and high adatom diffusion rate. The high supersaturation can overcome the high energy barrier for the growth of the epilayer on the substrate with dangling bonds, and the higher temperature promotes the diffusion of the adatoms, suppressing the nucleation on the vdW surface. Therefore, the low

(high) supersaturation of precursor and low (high) growth temperature contribute to the growth of nanowires (nanoplates) at the inner (edge) of the Bi_2O_2Se sheets.

Figure 3(a) is the optical microscope image of another $CsPbBr_3$–Bi_2O_2Se heterostructure. The micro-photoluminescence (μ-PL) spectra measured from the different positions on a $CsPbBr_3$ plate marked by the spots in Fig. 3(a) are shown in Fig. 3(b). Both μ-PL spectra exhibit a center wavelength of about 522 nm, agreeing well with the band edge emission of $CsPbBr_3$.[51] Differently, the position on the Bi_2O_2Se sheet (red dot) possesses the eight folder lower emission intensity relative to that on the mica, which indicates the significant PL quenching of $CsPbBr_3$ when contacts with Bi_2O_2Se. Figure 3(c) gives the PL mapping measured from the rectangle area marked in Fig. 3(a), with integrating the emission intensity near 522 nm. The whole region of the $CsPbBr_3$ plate on Bi_2O_2Se sheet shows much lower emission intensity than that on the mica (the dashed line denotes the edge of the Bi_2O_2Se sheet), which further confirms that the contact of $CsPbBr_3$ with Bi_2O_2Se can result in the PL quenching of $CsPbBr_3$.

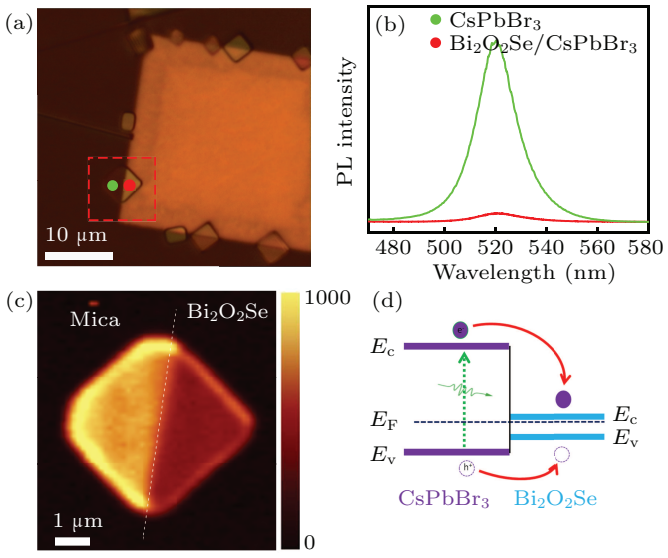


Fig. 3. (a) Optical microscope image of $CsPbBr_3$ nanoplate-Bi_2O_2Se nanosheet heterostructure. (b) PL spectra measured respectively from the positions marked with red and green dots in (a). (c) PL mapping of marked area with dotted line rectangle in (a). (d) The schematic of the band alignment diagram between $CsPbBr_3$ and Bi_2O_2Se.

Generally, the PL quenching in the semiconductor heterostructures is resulted from the charge transfer at the hetero-interface, which depends on their interfacial band alignment.[22] In order to obtain the information of band arrangement between $CsPbBr_3$ and Bi_2O_2Se in the heterostructure, UPS measurements were carried out. Combining the valence band spectra and second electron cutoff energy (E_{cut}) (see Fig. S6 for details), the work functions (W) of $CsPbBr_3$ and Bi_2O_2Se were estimated to be 5.31 eV and 4.69 eV, respectively, according to the formula of $W = h\nu - E_{cut}$ ($h\nu = 21.22$ eV, E_{cut} of $CsPbBr_3$ and Bi_2O_2Se are 15.91 eV and 16.53 eV, respectively), and the valence band maximum (VBM) of $CsPbBr_3$ and Bi_2O_2Se are 0.51 eV and 0.64 eV lower than their Fermi levels (E_F), respectively. Therefore, type-I band alignment should be formed at the hetero-interface based on the reported bandgaps of $CsPbBr_3$ (2.4 eV) and Bi_2O_2Se (0.8 eV),[22,48] which facilitates both the photo-generated electrons and holes in $CsPbBr_3$ injecting into Bi_2O_2Se and hence the PL quenching of $CsPbBr_3$ (see Fig. 3(d)). The UPS results can be further confirmed by the Kelvin probe measurements which show that W of $CsPbBr_3$ and Bi_2O_2Se are respectively 5.25 eV and 4.83 eV (see Fig. S7), agreeing with the values measured by UPS. Additionally, the excitation of 405 nm laser leaded to a decrease and increase in the potential of Bi_2O_2Se and $CsPbBr_3$, indicating the n- and p-type conduction of Bi_2O_2Se and $CsPbBr_3$, respectively.[22,47] These agree well with the relative energy difference between the E_F and the VBM measured by the UPS for Bi_2O_2Se and $CsPbBr_3$. Importantly, the efficient transfer of photo-generated carriers from $CsPbBr_3$ to Bi_2O_2Se promotes the carrier accumulation in Bi_2O_2Se, which is expected to improve the optoelectronic performance of the devices.[22]

To check the optoelectronic properties of the $CsPbBr_3$ nanoplate-Bi_2O_2Se nanosheet heterostructures, the dual electrode devices were fabricated with two Sn/Bi alloy foils contacting to the Bi_2O_2Se sheet (schematically shown in Fig. 4(a)). For comparison, the devices based on pristine Bi_2O_2Se sheets were also fabricated and studied with the same procedure (the optical microscope images of the devices are in Fig. S8). Figures 4(b) and 4(c) respectively show the I_{ds}–V_{ds} curves of the photodetectors based on pristine Bi_2O_2Se and $CsPbBr_3$-Bi_2O_2Se heterostructure, under dark and the illumination of 405 nm light with different optical power densities. The nearly linear dependence of I_{ds} on V_{ds} for both devices demonstrates the good ohmic contact between the electrodes and Bi_2O_2Se. The current enhancement with increasing the incident light power is attributed to the concentration increase of the photogenerated charge carriers in the Bi_2O_2Se channel. Responsivity (R) is a key performance parameter used to estimate the sensitivity of photodetectors and is defined as $R = I_{ph}/PS$, where I_{ph} is the photocurrent, P is the incident light density, and S is the effective area of the photodetector.[48] The blue squares and circles in Fig. 4(d) represent the power dependent R of the devices respectively based on $CsPbBr_3$–Bi_2O_2Se heterostructure and pristine Bi_2O_2Se sheet, measured at the bias of 3 V. The both devices exhibit an increase in R with reducing P. More importantly, the device of the heterostructure possesses higher R compared to that of the pristine Bi_2O_2Se sheet at the whole measured light intensity range. The former reaches the maximum R of 7.7 A/W at 60.25 W/m^2, while the latter only can achieve the R of

1.8 A/W at the same power. The specific detectivity (D^*) can be obtained according to its definition $D^* = \frac{R\sqrt{S}}{\sqrt{2eI_{dark}}}$, where e and I_{dark} are the elementary electron charge and the dark current, respectively (see the red squares and circles).[48] The photodetector based on the heterostructure has the highest D^* of 4.0×10^{10} Jones at $P = 60.25$ W/m^2, which is higher than the one based on the pristine Bi_2O_2Se sheet (3.6×10^{10} Jones). The lower increase of D^* than R resulted from the epitaxy of $CsPbBr_3$ on Bi_2O_2Se is due to the increased dark current of the PD based the heterostructures relative to that of the one based on pristine Bi_2O_2Se sheet (see Fig. S9). To further confirm the enhancement of the photoresponse by the formation of the heterostructure, the illumination-power normalized photocurrent spectra of the heterostructure device were in-situ measured respectively before and after removing the $CsPbBr_3$ nanoplates through soaking the device in distilled water (see Fig. S10(a)). Both spectra show broad response region extending from 375 nm to 1100 nm, which agrees well with the photodetectors based on Bi_2O_2Se.[48] Differently, a remarkable photocurrent increase can be observed at the wavelength shorter than 550 nm for the device based on the heterostructures, which agrees well with the band edge absorption of $CsPbBr_3$.[22] These results clearly exhibit that the epitaxy of $CsPbBr_3$ plate on the Bi_2O_2Se sheet can remarkably improve the optoelectronic performance of Bi_2O_2Se, which is attributed to the increased light absorption caused by the epitaxial $CsPbBr_3$ and the efficient transfer of photogenerated carriers from $CsPbBr_3$ to Bi_2O_2Se. To further prove that the increased photoresponse is resulted from $CsPbBr_3$, the optical absorption spectra of the pure Bi_2O_2Se and the heterostructures were measured (Fig. S10(b)). Both samples absorb the light initiating from about 1790 nm (0.69 eV), which agrees well with the band gap value ($\sim$ 0.8 eV) obtained by angle-resolved photoemission spectroscopy.[12] The heterostructure exhibits an abrupt increase of absorption at the wavelength of about 550 nm, which is consistent with the photocurrent spectrum in Fig. S10(a). Therefore, it can be concluded that the increased photoresponse of the device based on heterostructres is resulted from the increased light absorption by the epitaxial $CsPbBr_3$. Figure 4(e) gives the time-dependent current response (I_{ds}–t) of device of the heterostructure under the periodic on/off light illumination, exhibiting a highly stable and reproducible photocurrent response to the on/off light cycles. Figure 4(f) is the transient current response to a light pulse recorded by an oscilloscope. The rise and decay time can be respectively measured to be 4.4 ms and 2.8 ms, which indicates that the $CsPbBr_3$–Bi_2O_2Se heterostructure can be applied in the rapid response photodetectors.

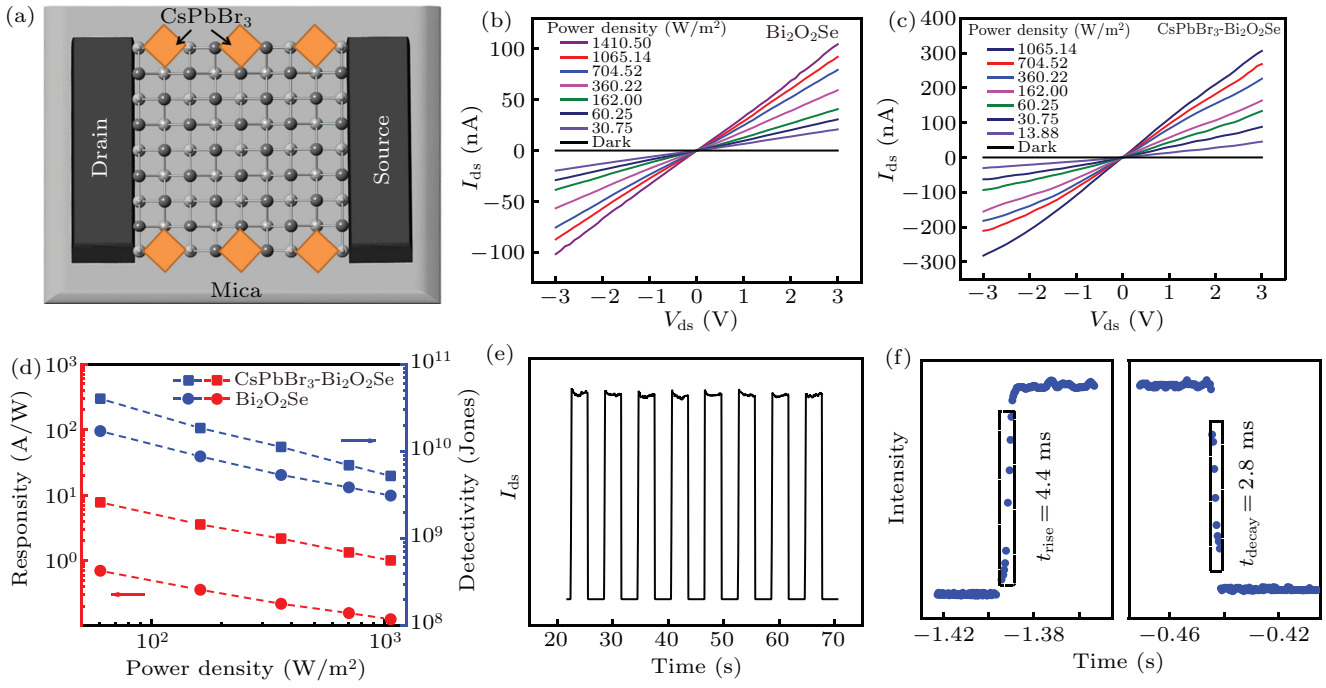


Fig. 4. (a) Schematic illustration of $CsPbBr_3$ nanoplate-Bi_2O_2Se heterostructure based device. (b) and (c) I_{ds}–V_{ds} curves of the photodetectors based on pristine Bi_2O_2Se and the heterostructure under dark and 450 nm illumination at different incident power densities. (d) The illumination power dependent responsivity and detectivity of the photodetectors based on the pristine Bi_2O_2Se and the heterostructure. (e) Time-dependent current response of the photodetector based on the heterostructure under repeated on/off light illumination. (f) Time-resolved light response photodetectors based on the heterostructures.

4. Conclusions

In summary, we have successfully synthesized $CsPbBr_3$ nanoplates-Bi_2O_2Se heterostructure by a two-step CVD growth method. The dangling bonds at the edge of Bi_2O_2Se sheet provide the initial nucleation site of $CsPbBr_3$, and the lattice match control their epitaxial relationships of $[200]_{Bi_2O_2Se} \| [110]_{CsPbBr_3}$ and $[110]_{Bi_2O_2Se} \| [200]_{CsPbBr_3}$.

The contact of $CsPbBr_3$ to Bi_2O_2Se results in the efficient photogenerated charge transfer from the former to the latter, which agrees with type-I band alignment at the heterointerface. Furthermore, the photodetectors based on the heterostructure possess the responsivity of 7.7 A/W at 60.25 W/m^2 that is 4 times higher than the ones based on pristine Bi_2O_2Se plates. This work provides an effective route to grown Bi_2O_2Se-based heterostructures which have the potential in the application in high-performance optoelectronic devices.

Acknowledgements

The authors are grateful to the National Natural Science Foundation of China (Grant No. 51772088) and Hunan Provincial Innovation Foundation for Postgraduate, China (Grant No. CX20200422), and thank Prof. Huigao Duan for the help of the PL measurements.

References

[1] Ross J S, Wu S, Yu H, Ghimire N J, Jones A M, Aivazian G, Yan J, Mandrus D G, Xiao D, Yao W and Xu X 2013 *Nat. Commun.* **4** 1474
[2] Yao J D and Yang G W 2021 *Nano Today* **36** 101026
[3] Liu Y, Huang Y and Duan X 2019 *Nature* **567** 323
[4] Liu C, Chen H, Wang S, Liu Q, Jiang Y G, Zhang D W, Liu M and Zhou P 2020 *Nat. Nanotechnol.* **15** 545
[5] Wang Y, Gao M, Wu J and Zhang X 2019 *Chin. Phys. B* **28** 018502
[6] Yue H, Hu A, Liu Q, Tian H, Hu C, Ren X, Chen N, Ge C, Jin K and Guo X 2021 *Chin. Phys. B* **30** 038502
[7] Zhou M, Zhao Y, Bian L, Zhang J, Yang W, Wu Y, Xing Z, Jiang M and Lu S 2021 *Chin. Phys. B* **30** 078506
[8] Wen H, Xiong L, Tan C, Zhu K, Tang Y, Wang J and Zhong X 2021 *Chin. Phys. B* **30** 057803
[9] Wu J, Tan C, Tan Z, Liu Y, Yin J, Dang W, Wang M and Peng H 2017 *Nano Lett.* **17** 3021
[10] Konstantatos G, Badioli M, Gaudreau L, Osmond J, Bernechea M, Garcia de Arquer F P, Gatti F and Koppens F H 2012 *Nat. Nanotechnol.* **7** 363
[11] Fu Q, Zhu C, Zhao X, Wang X, Chaturvedi A, Zhu C, Wang X, Zeng Q, Zhou J, Liu F, Tay B K, Zhang H, Pennycook S J and Liu Z 2019 *Adv. Mater.* **31** 1804945
[12] Yin J, Tan Z, Hong H, Wu J, Yuan H, Liu Y, Chen C, Tan C, Yao F, Li T, Chen Y, Liu Z, Liu K and Peng H 2018 *Nat. Commun.* **9** 3311
[13] Zhu C, Tong T, Liu Y, Meng Y, Nie Z, Wang X, Xu Y, Shi Y, Zhang R and Wang F 2018 *Appl. Phys. Lett.* **113** 061104
[14] Ghosh T, Samanta M, Vasdev A, Dolui K, Ghatak J, Das T, Sheet G and Biswas K 2019 *Nano Lett.* **19** 5703
[15] Khan U, Luo Y, Tang L, Teng C, Liu J, Liu B and Cheng H M 2019 *Adv. Funct. Mater.* **29** 1807979
[16] Wu Z, Liu G, Wang Y, Yang X, Wei T, Wang Q, Liang J, Xu N, Li Z, Zhu B, Qi H, Deng Y and Zhu J 2019 *Adv. Funct. Mater.* **29** 1906639
[17] Hong C, Tao Y, Nie A, Zhang M, Wang N, Li R, Huang J, Huang Y, Ren X, Cheng Y and Liu X 2020 *ACS Nano* **14** 16803
[18] Li T, Tu T, Sun Y, Fu H, Yu J, Xing L, Wang Z, Wang H, Jia R, Wu J, Tan C, Liang Y, Zhang Y, Zhang C, Dai Y, Qiu C, Li M, Huang R, Jiao L, Lai K, Yan B, Gao P and Peng H 2020 *Nat. Electron.* **3** 473
[19] Yang F, Wu J, Suwardi A, Zhao Y, Liang B, Jiang J, Xu J, Chi D, Hippalgaonkar K, Lu J and Ni Z 2020 *Adv. Mater.* **33** 2004786
[20] Chen Y, Ma W, Tan C, Luo M, Zhou W, Yao N, Wang H, Zhang L, Xu T, Tong T, Zhou Y, Xu Y, Yu C, Shan C, Peng H, Yue F, Wang P, Huang Z and Hu W 2021 *Adv. Funct. Mater.* **31** 2009554
[21] Zhao B, Bai S, Kim V, Lamboll R, Shivanna R, Auras F, Richter J M, Yang L, Dai L, Alsari M, She X J, Liang L, Zhang J, Lilliu S, Gao P, Snaith H J, Wang J, Greenham N C, Friend R H and Di D 2018 *Nat. Photonics* **12** 783
[22] Fan C, Xu X, Yang K, Jiang F, Wang S and Zhang Q 2018 *Adv. Mater.* **30** 1804707
[23] Ohno Y, Young D K, Beschoten B, Matsukura F, Ohno H and Awschalom D D 1999 *Nature* **402** 790
[24] Zhang Q, Liu H, Guo P, Li D, Fan P, Zheng W, Zhu X, Jiang Y, Zhou H, Hu W, Zhuang X, Liu H, Duan X and Pan A 2017 *Nano Energ.* **32** 28
[25] Yang C M, Chen T C, Verma D, Li L J, Liu B, Chang W H and Lai C S 2020 *Adv. Funct. Mater.* **30** 2001598
[26] Yang T, Li X, Wang L, Liu Y, Chen K, Yang X, Liao L, Dong L and Shan C X 2019 *J. Mater. Sci.* **54** 14742
[27] Luo P, Wang F, Qu J, Liu K, Hu X, Liu K and Zhai T 2020 *Adv. Funct. Mater.* **31** 2008351
[28] Xu Y, Zhou R, Yin Q, Li J, Si G and Zhang H 2021 *Chin. Phys. B* **30** 077304
[29] Li Y, Huang L, Li B, Wang X, Zhou Z, Li J and Wei Z 2016 *ACS Nano* **10** 8938
[30] Zhang Q, Zhu X, Li Y, Liang J, Chen T, Fan P, Zhou H, Hu W, Zhuang X and Pan A 2016 *Laser Photon. Rev.* **10** 458
[31] Luo P, Zhuge F, Wang F, Lian L, Liu K, Zhang J and Zhai T 2019 *ACS Nano* **13** 9028
[32] Li N, Wen Y, Cheng R, Yin L, Wang F, Li J, Shifa T A, Feng L, Wang Z and He J 2019 *Appl. Phys. Lett.* **114** 103501
[33] Chen T, Fan C, Zhou W, Zou X, Xu X, Wang S, Wan Q and Zhang Q 2019 *Appl. Phys. Express.* **12** 055005
[34] Adinolfi V and Sargent E H 2017 *Nature* **542** 324
[35] Guo H W, Hu Z, Liu Z B and Tian J G 2020 *Adv. Funct. Mater.* **31** 2007810
[36] Xu X, Fan C, Wang Y, Qi Z, Dai B, Jiang H, Wang S and Zhang Q 2020 *Phys. Status Solidi-Rapid Res. Lett.* **14** 2000384
[37] Zhai X, Xu X, Peng J, Jing F, Zhang Q, Liu H and Hu Z 2020 *ACS Appl. Mater. Interfaces* **12** 24093
[38] Zheng W, Feng W, Zhang X, Chen X, Liu G, Qiu Y, Hasan T, Tan Pand Hu P A 2016 *Adv. Funct. Mater.* **26** 2648
[39] Wen Y, Yin L, He P, Wang Z, Zhang X, Wang Q, Shifa T A, Xu K, Wang F, Zhan X, Wang F, Jiang C and He J 2016 *Nano Lett.* **16** 6437
[40] Zhao L, Gao Y, Su M, Shang Q, Liu Z, Li Q, Wei Q, Li M, Fu L, Zhong Y, Shi J, Chen J, Zhao Y, Qiu X, Liu X, Tang N, Xing G, Wang X, Shen B and Zhang Q 2019 *ACS Nano* **13** 10085
[41] Wang S, Yu J, Zhang M, Chen D, Li C, Chen R, Jia G, Rogach and Yang X 2019 *Nano Lett.* **19** 6315
[42] Fakharuddin A, Shabbir U, Qiu W, Iqbal T, Sultan M, Heremans P and Lukas Schmidt L 2019 *Adv. Mater.* **31** 1807095
[43] Fang Q, Shang Q, Zhao L, Wang R, Zhang Z, Yang P, Sui X, Qiu X, Liu X, Zhang Q and Zhang Y 2018 *J. Phys. Chem. Lett.* **9** 1655
[44] Li H, Zheng X, Liu Y, Zhang Z and Jiang T 2018 *Nanoscale* **10** 1650
[45] Noh T, Shin H, Seo C, Kim J, Youn J, Kim J, Lee K and Joo 2019 *J. Nano Res.* **12** 405
[46] Zhang L, Shen S, Li M, Li L, Zhang J, Fan L, Cheng F, Li C, Zhu M,Kang Z, Su J, Zhai T and Gao Y 2019 *Adv. Opt. Mater.* **7** 1801744
[47] Fan C, Zhang Q, Zhu X, Zhuang X and Pan A 2015 *Sci. Bull.* **60** 1674
[48] Xu S, Fu H, Tian Y, Deng T, Cai J, Wu J, Tu T, Li T, Tan C, Liang Y, Zhang C, Liu Z, Liu Z, Chen Y, Jiang Y and Yan B and Peng H 2020 *Angew. Chem.* **59** 17938
[49] Fan C, Dai B, Liang H, Xu X, Qi Z, Jiang H, Duan H and Zhang Q 2021 *Adv. Funct. Mater.* **31** 2010263
[50] Zheng W, Feng W, Zhang X, Chen X, Liu G, Qiu Y, HasanT, Tan P and Hu P 2016 *Adv. Funct. Mater.* **26** 2648
[51] Fan C, Bi K, Shu Z, Xu X, Dai B, Wang S, Qi Z, Wei J, Duan H and Zhang Q 2020 *J. Phys. D-Appl. Phys.* **53** 235105
[52] Liu X, Li R, Hong C, Huang G, Pan D, Ni Z, Huang Y, Ren X, Cheng Y and Huang W 2019 *Nanoscale* **11** 20707